



HAL
open science

Modeling longitudinal dispersion in variable porosity porous media : control of velocity distribution and microstructures

Philippe Gouze, Alexandre Puyguraud, Thierry Porcher, Marco Dentz

► To cite this version:

Philippe Gouze, Alexandre Puyguraud, Thierry Porcher, Marco Dentz. Modeling longitudinal dispersion in variable porosity porous media : control of velocity distribution and microstructures. *Frontiers in Water*, 2021. hal-03396794v1

HAL Id: hal-03396794

<https://hal.umontpellier.fr/hal-03396794v1>

Submitted on 22 Oct 2021 (v1), last revised 25 Oct 2021 (v2)

HAL is a multi-disciplinary open access archive for the deposit and dissemination of scientific research documents, whether they are published or not. The documents may come from teaching and research institutions in France or abroad, or from public or private research centers.

L'archive ouverte pluridisciplinaire **HAL**, est destinée au dépôt et à la diffusion de documents scientifiques de niveau recherche, publiés ou non, émanant des établissements d'enseignement et de recherche français ou étrangers, des laboratoires publics ou privés.

Modeling longitudinal dispersion in variable porosity porous media : control of velocity distribution and microstructures.

Philippe Gouze^{1,*}, Alexandre Puyguiraud², Thierry Porcher¹ and Marco Dentz²

¹*Geoscience Montpellier, CNRS, Université de Montpellier, Montpellier, France*

²*Spanish National Research Council (IDAEA-CSIC), Barcelona, Spain*

Correspondence*:

Philippe.Gouze@Umontpellier.fr

2 ABSTRACT

3 Hydrodynamic dispersion process in relation with the geometrical properties of the porous media
 4 are studied in two sets of 6 porous media samples of porosity θ ranging from 0.1 to 0.25. These
 5 two sets of samples display distinctly different evolutions of the microstructures with porosity but
 6 share the same permeability trend with porosity. The methodology combines three approaches.
 7 First, numerical experiments are performed to measure pre-asymptotic to asymptotic dispersion
 8 from diffusion-controlled to advection-controlled regime using Time-Domain Random Walk solute
 9 transport simulations. Second, a porosity-equivalent network of bonds is extracted in order to
 10 measure the geometrical properties of the samples. Third, the results of the direct numerical
 11 simulations are interpreted as a Continuous Time Random Walk (CTRW) process controlled by
 12 the flow speed distribution and correlation. These complementary modelling approaches allows
 13 evaluating the relation between the parameters of the conceptual transport process embedded in
 14 the CTRW model, the flow field properties and the pore-scale geometrical properties. The results
 15 of the direct numerical simulations for all the 12 samples show the same scaling properties of the
 16 mean flow distribution, the first passage time distribution and the asymptotic dispersion versus the
 17 Péclet number than those predicted by the CTRW model proposed by Puyguiraud et al. (2021). It
 18 allows predicting the asymptotic dispersion coefficient D^* from $Pe = 1$ to the largest values of
 19 Pe expected for laminar flow in natural environments ($Pe \approx 4000$). $D^* \propto Pe^{2-\alpha}$ for $Pe \geq Pe^{crit}$,
 20 where α can be inferred from the Eulerian flow distribution and Pe^{crit} depends on porosity. The
 21 Eulerian flow distribution is controlled by the distribution of fractions of fluid flowing at each of the
 22 pore network nodes and thus is determined mainly by the distribution of the throat radius and the
 23 coordination number. The later scales with the number of throats per unit volume independently
 24 on the porosity. The asymptotic dispersion coefficient D^* decreases when porosity increases for
 25 all Péclet values larger than 1 due to the increase with porosity of both α and the flow speed
 26 decorrelation length.

1 INTRODUCTION

27 Modeling transport of solute in porous media is a prerequisite for many environmental and engineering
 28 applications, ranging from aquifers contaminant risk assessment to industrial reactors, filters and batteries
 29 design. The solutes can be pollutants, reactants and products involved in solute-solute or solute-mineral
 30 reactions, but also (bio-)nanoparticles or nutrients involved in the growth of bio-mass. The mechanism
 31 under consideration is the spatial dispersion which leads to the spreading and the mixing of dissolved

32 chemicals, thus controlling the potential reactions in the flowing fluid and between the fluid and the porous
 33 media (Bear, 1972; Brenner and Edwards, 1993; Dentz et al., 2011). The dispersion process has been,
 34 and still is, a largely studied topic in the field of geosciences because rocks at depth are, as a general
 35 rule, porous media saturated with fluid(s) that move due to natural or artificial pressure gradients, and
 36 display a large spectrum of heterogeneities. In all these domains, reliable predictive models that can be
 37 parameterized by direct measurements are necessary, for example, to monitor and assess risks linked to
 38 the use of underground water resources, or in the course of industrial operations, such as hydrocarbon
 39 exploitation and CO₂ or underground nuclear waste storage.

40 Hydrodynamic dispersion is the macroscopic result of the mass transfers by diffusion and advection
 41 that occurs at the pore scale (Whitaker, 1967; Sahimi, 2011; De Anna et al., 2013). Together, diffusion
 42 and advection of solute produce a large spectrum of dispersion features because (natural) porous media
 43 display complex structures inducing a large diversity of velocity fields, and thus distinctly different speed
 44 distributions and spatial correlations. Probably the most obvious behavior that illustrates the complexity
 45 of dispersion mechanisms in porous media is the variably-lasting pre-asymptotic dispersion regime that
 46 cannot be modeled by a single Fickian dispersion coefficient. Pre-asymptotic, or non-Fickian, dispersion
 47 is commonly observed in laboratory experiments (Moroni and Cushman, 2001; Levy and Berkowitz,
 48 2003; Seymour et al., 2004; Morales et al., 2017; Carrel et al., 2018; Souzy et al., 2020), and numerical
 49 simulations (Bijeljic et al., 2011, 2013; De Anna et al., 2013; Icardi et al., 2014; Kang et al., 2014; Li
 50 et al., 2018; Puyguiraud et al., 2019c). It is characterized by heavy-tailed arrival time distributions $f_t(t)$
 51 and super-diffusive growth of the longitudinal displacement variance $\sigma^2(t)$. For a given porous medium,
 52 the duration of the non-Fickian regime is controlled by solute particles that move the slowest, which
 53 emphasizes the determinant role of both the regions where the velocity is low and the tortuosity of the
 54 flow paths. Asymptotically dispersion converges toward Fickian behavior, characterized by the constant
 55 longitudinal dispersion coefficient D^* (Bear, 1972; Brenner and Edwards, 1993).

56 Evaluating the longitudinal asymptotic dispersion coefficient D^* is a fundamental issue, because most
 57 operational modeling tools have been constructed around the Fickian advection-dispersion equation that
 58 reads for transport in the direction of the mean flow, here the z -direction, (Bear, 1972):

$$59 \quad \frac{\partial \theta c(z, t)}{\partial t} - \frac{\partial}{\partial z} \left[\theta D^* \frac{\partial c(z, t)}{\partial z} + u_z(z) c(z, t) \right] = 0, \quad (1)$$

61 where c is the solute concentration, θ is the connected porosity, $u_z = \theta \langle v_z \rangle$ denotes Darcy's velocity, with
 62 $\langle v_z \rangle$ being the mean pore velocity.

63 Many experimental studies and mathematical developments on dispersion using mainly simple porous
 64 media have been performed since the pioneering works of Danckwerts (1953). The reader will find an
 65 exhaustive review of the different results and models of both longitudinal and transverse dispersion in
 66 Delgado (2006). A main well observed feature of longitudinal dispersion D^* is its non-linear increase
 67 with the mean flow velocity. It is recognized since the pioneering works of Saffman (1959) and then Bear
 68 (1972). It is generally expressed in terms of D^*/d_m versus the Péclet number $Pe = \langle v_e \rangle \ell / d_m$, where ℓ is a
 69 characteristic length, d_m is the molecular diffusion coefficient and $\langle v_e \rangle$ is the mean Eulerian flow speed
 70 ($v_e = \sqrt{v_x^2 + v_y^2 + v_z^2}$, with v_i denoting the flow velocity component i , see Section 2.2). Simulations in
 71 networks of constant velocity tubes (Sahimi and Imdakm, 1988) of radius r following distributions such as

72 $P(r) \propto re^{-r^2}$ (Chatzis and Dullien, 1985) indicated a relation of the form

73
$$D^*/d_m \propto Pe^\beta, \quad (2)$$

75 with $\beta = 1.2 \mp 0.1$ (Sahimi, 2011), while for instance $\beta = 2$ in a single tube (Taylor, 1953). For infinite
 76 Pe , experimental particle tracking results (e.g. Souzy et al., 2020) give the relation $D^*/d_m \approx Pe$, where
 77 the characteristic length ℓ is of the order of the pore length. However, it is worth noticing that in Souzy
 78 et al. (2020)'s experiments the lowest velocities cannot be measured because they use finite-size particles
 79 that cannot access to the vicinity of the solid. Interestingly, the behavior (2) with $\beta \simeq 1.2$ was cited in
 80 numerous studies concerning bead-packs and homogeneous sand-packs for intermediate Péclet numbers
 81 (Pfannkuch, 1963; Han et al., 1985; Seymour and Callaghan, 1997; Sahimi et al., 1986; Bijeljic et al., 2004).
 82 For instance, particle tracking simulations in pore-networks reported in Bijeljic and Blunt (2006) gave
 83 $\beta = 1.2$, for $Pe < 400$ and $\beta = 1$, for $Pe > 400$. Conversely, similar numerical simulations (using random
 84 walk particle tracking) performed by Puyguiraud et al. (2021) using digitized images of consolidated
 85 sandstone, gave a value of $\beta = 1.65$ for $10 \leq Pe \leq 10^5$. The few experimental data on rocks (obviously
 86 more heterogeneous than bead-packs) displayed a broader range of behaviors; for example Kinzel and Hill
 87 (1989) reported $1.30 \leq \beta \leq 1.33$. However, it is worth noticing that evaluating dispersion in rocks, for a
 88 large range of Pe values, either at laboratory or field scale from tracer tests is challenging. For instance,
 89 controlling the boundary conditions and verifying that the tracer is conservative are some of the known
 90 issues that may introduce errors in the estimation. Yet, the main issue is probably linked to the fact that, by
 91 definition, the experimental results are interpreted using the Fickian model, whereas it is difficult to prove
 92 that dispersion is asymptotic without being able to measure the tracer breakthrough curves over several
 93 orders of magnitude in order to capture the low speed fraction of the solute transport (Gouze et al., 2008).
 94 We will show in Section 3.4 that measuring asymptotic dispersion for large values of Pe in natural porous
 95 media is in fact virtually impossible using cm- or even meter-scale experiments.

96 While measuring dispersion experimentally is burdensome, modeling approaches are now mature to
 97 perform numerical experiments. Direct numerical simulations (DNS) are unique tools for investigating
 98 both the pre-asymptotic and the asymptotic behavior in a common frame. They can be used to accurately
 99 measure D^* , but also to study the mechanisms that produce dispersion in relation with the measurable
 100 (average) properties of the material, and to test upscaling theories. Recent works (Bijeljic and Blunt,
 101 2006, 2007; De Anna et al., 2013; Puyguiraud et al., 2019a, 2021) showed that hydrodynamic transport in
 102 porous media can be adequately conceptualized and modeled by a continuous time random walk (CTRW)
 103 that models streamwise transport through particle transitions over fixed spatial distance with a transition
 104 time given by the local flow speed and diffusion. The spatial distance at which particles speed changes
 105 corresponds to the decorrelation distance ℓ_c of the mean flow speed. The CTRW integrates in a statistical
 106 framework parameters that are similar to the classical representation of porous media as a network of
 107 throats and pores. As such one can be tempted to investigate how ℓ_c , which is a major ingredient of the
 108 CTRW model, is related to the topological and geometrical properties of the real 3-dimensional pore
 109 network. Moreover, the CTRW model predicts that asymptotic dispersion is controlled by the dispersion
 110 evolution during the pre-asymptotic regime which itself is controlled by the flow speed distribution. How
 111 the later is related to the properties of the pore network is a further issue that requires investigation.

112 The main objective of the present study, is to investigate the relation between the longitudinal dispersion
 113 D^* (and its evolution with the mean flow rate) and the porous media microstructural properties in the frame
 114 of the theory proposed by Puyguiraud et al. (2021) which gives a generalized explanation of longitudinal

115 dispersion (from pre-asymptotic to asymptotic regimes) and a formal relation between dispersion and the
 116 properties of the flow field (velocity distribution, velocity spatial decorrelation and flow path tortuosity).

117 The core of this study is a set of about 150 numerical experiments designed to measure pre-asymptotic
 118 to asymptotic dispersion from diffusion-controlled to advection-controlled regime in 12 sandstone-like
 119 samples of porosity ranging from 10 to 25%. For that, one first computes the steady-state Stokes flow field
 120 from which, the flow speed distribution and the decorrelation distance as well as advective tortuosity are
 121 derived. Then, the direct numerical simulation (DNS) of solute transport at pore scale, involving diffusion
 122 and advection, are performed using Time-Domain Random Walk (TDRW). The dispersion mechanisms are
 123 characterized from the time-resolved particles displacement variance and the first passage time distribution
 124 (FPT) given as outputs of the TDRW simulations. In parallel, the geometrical properties of the porous
 125 samples are evaluated from the computation of the bonds network model (BNM) for each of the samples,
 126 that is obtained from the medial axis transform, or skeletonization, of the connected porosity. This gives
 127 us the unique opportunity to characterize the topology of the connected porosity including the number of
 128 throats (bonds) and pores (network nodes) and the coordination (number of throats per pore), as well as
 129 the throat radius and length. Then, the results of the direct numerical simulations are analyzed in the light
 130 of the CTRW theory proposed by Puyguiraud et al. (2021) which provides quantitative links between the
 131 tail behaviors of the FPT distribution $f_t(t)$, the distribution of flow speeds v_e , the particles displacement
 132 variance $\sigma^2(t)$ and the asymptotic dispersion coefficient D^* scaling with the Pe value.

133 The methodology, including the conceptual and numerical tools used in this study are detailed in Section 2.
 134 The geometrical and topological characteristics of the samples and the flow field properties are presented
 135 in Section 3. The results of the direct numerical simulation of solute transport and the calculation of the
 136 dispersion coefficient for a large range of values of Pe are discussed in Section 3.4. The conclusions of this
 137 study are exposed in Section 4.

2 METHODOLOGY

138 2.1 Porous media samples

139 The porous media are binary images made of 480^3 regular voxels (cubes) that are either void or solid.
 140 The first set of 6 samples, noted $FSxx$, where xx is replaced by the porosity value expressed in percent (ex:
 141 $FS13$ for the sample with $\theta=0.13$) was downloaded from the Digital Rocks Portal (Berg, 2016a). They
 142 were generated with the commercial software e-Core following a methodology described in (Oren, 2002)
 143 in order to mimic Fontainebleau sandstone at different porosity (Berg, 2016b). The op. cit. author indicated
 144 that they use identically parameterized silica grain sedimentation and compaction processes typical for
 145 Fontainebleau sandstones, the different porosity values (0.10, 0.13, 0.15, 0.21 and 0.25) being obtained by
 146 varying the amount of silica cement. As such, this process mimics the progressive diagenetic cementation
 147 by silica precipitation (from $FS25$ to $FS10$) of an initially poorly cemented sandstone. Conversely, we
 148 made the second set of samples by step-by-step homogeneous erosion of the solid phase starting from
 149 $FS10$. By removing 1 to 6 layers of solid at the solid-void interface we obtain 6 samples, denoted $FSDxx$
 150 of porosity 0.12, 0.15, 0.17, 0.20, 0.23 and 0.25. This process mimics homogeneous dissolution of the
 151 silica material. The top panel in Figure 1 displays the three-dimensional structure of the lowest porosity
 152 sample $FS10$, and the highest porosity samples $FS25$ and $FSD25$. It can be qualitatively appraised that
 153 the cement precipitation model used to construct $FS25$ increases the number of pores compared $FS10$,
 154 while the pore size is kept roughly similar. In contrast, the dissolution process producing $FS25$ from $FS10$
 155 acts as increasing strongly the pore size, while the number of pores remains roughly unchanged. This set of
 156 sample is viewed as ideal for investigating dispersion of end-members of natural sandstones.

157 **2.2 Flow**

158 Flow simulations are performed on the three-dimensional binary images. The mesh used for solving the
 159 flow is obtained by dividing each of the image voxels by 3 in each of the directions so that 1 voxel of the
 160 raw image is represented by 9 cubic cells of size $\Delta x = \Delta y = \Delta z = 2.85 \times 10^{-6}$ m. This procedure is
 161 applied for improving the resolution of the flow field in the smallest throats (Gjetvaj et al., 2015). The
 162 resulting discretization for the regular grid consists of 960^3 cubic cells. We are considering steady-state
 163 flow of an non-compressible Newtonian fluid at low Reynolds number so that the pore-scale flow velocity
 164 $\mathbf{v}(\mathbf{x})$ is given by the Stokes equation

165
$$\mu \nabla^2 \mathbf{v}(\mathbf{x}) - \nabla p(\mathbf{x}) = 0, \quad (3)$$

167 where $p(\mathbf{x})$ is the fluid pressure. Stokes flow is solved using the finite volume SIMPLE (SemiImplicit
 168 Method for Pressure Linked Equations algorithm) scheme implemented in the SIMPLEFOAM solver of
 169 the OpenFOAM platform (Weller et al., 1998). Twenty layers are added at the inlet and outlet in order to
 170 minimize boundary effects (Guibert et al., 2016). The main flow direction is considered in the z -direction
 171 all over this study. We prescribe 1) a macroscopic pressure gradient $\nabla^* p$ between the inlet ($z = 0$) and
 172 the outlet ($z = Lz$) boundary conditions such that the Reynolds number Re is smaller than 10^{-6} , i.e.
 173 laminar flow and 2) no-slip conditions at the void-solid interfaces and at the remaining boundaries of the
 174 sample. After convergence, that is, once the normalized residual of the pressure and velocity components
 175 is below 10^{-5} between two consecutive steps, we extract the components of the velocity at the voxel
 176 interfaces (v_x, v_y, v_z). The results of the flow simulations allow us to extract the three properties that
 177 control dispersion according to Puyguiraud et al. (2019b): 1) the Eulerian speed distribution $p_e(v)$ 2)
 178 the decorrelation distance ℓ_c and 3) the advective tortuosity χ_a . These fundamental flow properties are
 179 respectively displayed in Figures 5, 6, and 7, and discussed in Section 3.

180 **2.3 Solute transport**

181 Pore-scale hydrodynamic transport is classically modeled by the advection-diffusion equation

182
$$\frac{\partial c(\mathbf{x}, t)}{\partial t} - \nabla \cdot [d_m \nabla + \mathbf{v}(\mathbf{x})] c(\mathbf{x}, t) = 0, \quad (4)$$

184 where $c(\mathbf{x}, t)$ is the solute concentration at position \mathbf{x} and time t , d_m is the molecular diffusion coefficient
 185 which is set equal to $d_m = 10^{-9}$ m²/s, and $\mathbf{v}(\mathbf{x})$ is the flow velocity at position \mathbf{x} which is obtained by
 186 solving the Stokes problem (see Section 2.2). Here we use the time domain random walk (TDRW) method
 187 that is based on a finite volume discretization of Equation (4) (Delay et al., 2005). A detailed description
 188 of the TDRW method, its derivation and implementation using voxelized binary images can be found
 189 in Dentz (2012) and Russian et al. (2016); the main features of the method are given below. A study of the
 190 performance and accuracy of the TDRW method for a large range of values of the Péclet number can be
 191 found in (Gouze et al., 2021). The domain discretization used for transport is that used for computing the
 192 flow, i.e., 960^3 cubic voxels .

193 The TDRW method is a grid-based method that models the displacement of particles in space and time
 194 according to the master equation that results from a finite volume discretization of the advection-diffusion
 195 equation. The ensemble average of the particle displacement gives the solution of the transport equation.
 196 A particle transition corresponds to a single transition of a constant length $\xi = \Delta x$ from the center of a
 197 voxel j to the center of one of the 6 face-neighboring voxels i . The direction and the transition duration are
 198 random variables ruled by the local values of the fluid velocity at the voxel interface embedded into the

199 local coefficients b_{ij} (Russian et al., 2016)

$$200 \quad b_{ij} = \frac{d_m}{\xi^2} + \frac{|v_{ij}|}{2\xi} \left(\frac{v_{ij}}{|v_{ij}|} + 1 \right), \quad (5)$$

201 where v_{ij} is the velocity component of \mathbf{v}_j in the direction of voxel i , $v_{ij} = \mathbf{v}_j \cdot \boldsymbol{\xi}_{ij}$. Voxel i is downstream
 202 from voxel j if $v_{ij} > 0$, as a convention. The velocity at the solid-void interface is zero and $d_m = 0$ if
 203 voxel i is a solid voxel. The recursive relations that describe the random walk from position \mathbf{x}_j to position
 204 \mathbf{x}_i of a given particle transition n is

$$205 \quad \mathbf{x}_i(n+1) = \mathbf{x}_j(n) + \boldsymbol{\xi}, \quad t(n+1) = t(n) + \tau_j. \quad (6)$$

206 The probability p_{ij} for a transition of length ξ from voxel j to voxel i is

$$207 \quad p_{ij} = \frac{b_{ij}}{\sum_{[jk]} b_{kj}}, \quad (7)$$

208 where $\sum_{[jk]}$ denotes the summation over the nearest neighbors of voxel j . The transition time τ_j is
 209 independent on the transition direction and is exponentially distributed $\psi_{\tau_j}(t) = \bar{\tau}_j \exp(-t/\bar{\tau}_j)$ with $\bar{\tau}_j$
 210 the mean transition time from voxel j ;

$$211 \quad \bar{\tau}_j = \frac{1}{\sum_{[jk]} b_{kj}}. \quad (8)$$

212 The algorithm consists in computing once the probability p_{ij} (7) and the mean transition time $\bar{\tau}_j$ (8) for
 213 each of the voxels belonging to the pore space and then solving the random walk (6) in which the direction
 214 for each particle transition is drawn from the p_{ij} vector and the transition time is drawn from the exponential
 215 distribution of mean $\bar{\tau}_j$.

216 2.3.1 Simulation setup

217 For each sample, we performed simulations for different values of the Péclet number. The Péclet number
 218 is defined as $Pe = \langle v_e \rangle \lambda / d_m$ where λ is the mean throat length that is displayed for the 12 samples in
 219 Figure 2 and ranges from $6.5 \times 10^{-5} \text{m}$ to $8.8 \times 10^{-5} \text{m}$. The different flow fields used for the TDRW
 220 simulations at different Péclet numbers are obtained by multiplying the raw flow field resulting from the
 221 Stokes simulation by a constant.

222 A *pulse* of constant concentration at the sample inlet ($z = 0$) is applied at $t = 0$ by locating particles
 223 in a flux weighted injection mode. Note that the *pulse* is formally an exponential distribution function
 224 of characteristic time $\tau_j|_{z=0}$ whose mean value is negligible compared to the mean time required for the
 225 particles to move through the sample (Russian et al., 2016). Flux weighted injection means that the number
 226 of particles injected at a location is proportional to the local velocity. This corresponds to a constant
 227 concentration Dirichlet boundary condition. Particles that reach the sample outlet with a speed v_{out} are
 228 reinjected randomly at the inlet plane at a position \mathbf{x} satisfying the condition $|\mathbf{v}_x - v_{out}| \ll \langle v \rangle$.

229 The distribution (PDF) of first passage times at a given distance Z from the injection location, that
 230 denotes the solute breakthrough curve (BTC) usually measured in laboratory or field tracer tests, is noted
 231 $f_t(t)$ (Figure 8). The apparent longitudinal dispersion coefficient $D(t)$ is evaluated from the displacement
 232 variance $\sigma_z^2(t)$ of the particles (Fischer, 1966):

$$D(t) = \frac{1}{2} \frac{d\sigma_z^2(t)}{dt}, \quad (9)$$

233 with $\sigma_z^2(t) = \langle (z(t) - \langle z \rangle)^2 \rangle - \langle z(t) - \langle z \rangle \rangle^2$. The asymptotic longitudinal dispersion coefficient $D^* =$
 234 $\sigma_z^2(t)/2t$ is obtained for $t > t^*$, where t^* is the time required for all the particles to sample the entire
 235 heterogeneity, i.e. when $\sigma_z^2(t) \sim t$ (see for example Figure 10).

236 2.4 The equivalent bond network model

237 We compute the bond network model (BNM) for each of the *FS* and *FSD* samples in order to extract
 238 the geometrical and topological characteristics of the connected porosity. The methodology to obtain the
 239 network representation of the connected porosity of the sample includes two main steps. The first one is the
 240 extraction of the void space skeleton which is the one-dimensional continuous object centrally located (and
 241 spatially referenced) inside the pore space. The skeleton can be computed using different approaches; here we
 242 used a thinning algorithm inspired from the works of Lee et al. (1994) that provides the local medial-axis.
 243 The coordinate of the skeleton is known with a spatial resolution equivalent to that of the original 3D-image
 244 and associated with the local hydraulic radius r_l normal to the local medial axis that is evaluated using a
 245 pondered 45 degree multi-ray method. Thus, the skeleton keeps the relevant geometrical and topological
 246 features of the pore space (Siddiqi and Pizer, 2008). The second step consists in transforming the skeleton
 247 into a network of bonds and nodes that connect three or more bonds. This yields an irregular lattice. The
 248 length λ of a given bond is the sum of the length of the skeleton components used to build this bond,
 249 so that the local tortuosity of the skeleton is embedded into λ . For each bond, the radius r_h is obtained
 250 from the harmonic means (noted $\langle \rangle_H$) of the local conductance, so that $r_h = (\langle r_l \rangle_H)^{1/4}$. The algorithm is
 251 non-parametric; there is no assumption on any of the characteristics of obtained the lattice.

252 2.5 Upscaled CTRW model

253 Puyguiraud et al. (2021) propose a continuous time random walk (CTRW) model that describes transport
 254 through particle transitions over the length ℓ_c with a transition time that is given by the local flow speed
 255 and diffusion. The central assumption of this model is that transition times at subsequent CTRW steps are
 256 independent identically distributed random variables. Furthermore, it is assumed that particles move at the
 257 mean pore velocity, that is, it is assumed that during a transition particles are able to diffusively sample the
 258 velocities across pore conducts. The scale ℓ_c is set equal to the decorrelation distance of particle speeds so
 259 that subsequent particle speeds can be considered statistically independent. The distribution of Eulerian
 260 mean flow speeds $p_m(v)$ is obtained from the Eulerian speed PDF as

$$p_m(v) = -2v \frac{dp_e(2v)}{dv}. \quad (10)$$

261 As particles move at equidistant spatial steps, they sample flow speeds in a flux-weighted manner. This
 262 is due to the fact that particles are distributed at pore intersections according to the relative downstream
 263 fluxes. Thus, the distribution $p_v(v)$ of subsequent particle speeds are related to the distribution of Eulerian
 264 flow speeds through flux-weighting as (Puyguiraud et al., 2021)

$$p_v(v) = \frac{vp_m(v)}{\langle v_m \rangle}. \quad (11)$$

At each turning point of the CTRW, particles are assigned a random speed from $p_v(v)$. The particle transition time distribution $\psi(t)$ reflects both advection and diffusion. It is cut-off at times larger than $\tau_D = \ell_c^2/d_m$, the diffusion time over the decorrelation distance. For times small compared to the cut-off time, $\psi(t)$ can be approximated by

$$\psi(t) = \frac{\ell_c^2}{t^3 \langle v_m \rangle} p_m(\ell_c/t). \quad (12)$$

265 At times larger than τ_D it is cut-off exponentially fast.

266 The flow speed distribution is at the center of the transport process. In porous media, such as rocks, the
 267 mean flow speed can often be approximated by a Gamma-type distribution (Dentz et al., 2018; Puyguiraud
 268 et al., 2019b; Souzy et al., 2020) and displays a power-law scaling $p_e(v) \sim v^{\alpha-1}$ for $v < \langle v_m \rangle$. For sphere
 269 packs and simple structures such as sand-pack the linear flow profile close to the grains (due to the no-slip
 270 boundary condition) implies that $p_e(v)$ is flat at low velocities, so that $\alpha \simeq 1$ (Dentz et al., 2018). In more
 271 heterogeneous porous media, other values of α are expected. For example, Puyguiraud et al. (2021) found
 272 $\alpha \approx 0.35$ for a Berea sandstone sample. For such Gamma-type distributions, $p_e(v) \sim v^{\alpha-1}$ at small flow
 273 speeds, $\psi(t)$ behaves for high Péclet numbers as $\psi(t) \sim t^{-2-\alpha}$ before the exponential cut-off at times
 274 larger than τ_D . The tortuosity of particle trajectories in this framework is given by the ratio of the mean
 275 asymptotic particle speed $\ell_c/\langle \tau \rangle \equiv \langle v_e \rangle$ (where $\langle \tau \rangle$ denotes the particle mean travel time) and the mean
 276 streamwise flow velocity $\langle v_z \rangle$. Furthermore, for this type of flow speed distributions, the CTRW approach
 277 predicts some further interesting scaling laws that can be verified from direct numerical simulations. The
 278 behavior of particle breakthrough curves $f(t, Z)$ at a control plane located at the streamwise location Z is
 279 analogous to the behavior of $\psi(t)$. They show a power-law dependence as $f(t, Z) \sim t^{-2-\alpha}$ if $Z/v_z \ll \tau_D$
 280 (i.e., the peak time is much smaller than the cut-off time), and exponential decay for times larger than the
 281 cut-off time τ_D . The predicted dependence of the asymptotic longitudinal dispersion coefficients on the
 282 Péclet number is for $Pe \gg 1$

$$\frac{D^*}{d_m} \sim Pe^{2-\alpha} \quad (13)$$

for $0 < \alpha < 1$ and

$$\frac{D^*}{d_m} \sim Pe \ln Pe \quad (14)$$

283 for $\alpha = 1$, see also Saffman (1959) and Koch and Brady (1985).

284 To sum-up, this upscaled model, constructed on the representation of the hydrodynamic transport as a
 285 CTRW process in a network of bonds, is fully constrained, for any values of $Pe > 1$ by the knowledge of
 286 the distribution of Eulerian flow speeds $p_e(v)$ and the decorrelation distance ℓ_c of particle speeds.

287 From here one can recognize on one hand the complementarity of the BNM and the DNS to explore the
 288 relation between the dispersion and the pore network characteristics, and on the other hand the conceptual
 289 framework that links the CTRW model and the BNM representation of the porous medium. This emphasizes
 290 the possibility of 1) relating the distribution of the Eulerian flow speed to the large scale transport behavior
 291 and 2) characterizing dispersion for different porous media based on the knowledge of the flow speed
 292 distribution. Indeed, the BNM gives us the information on the real topology of the pore network as
 293 well as the distribution and the average of bond properties (radius and length), while the DNS provides
 294 the information on the flow field (speed distribution and decorrelation distance as well as the advective
 295 tortuosity).

3 PORE NETWORK PROPERTIES, FLOW FIELDS AND DISPERSION

296 The top row in Figure 1 illustrates the 3-dimensional structure of sample *FS10* ($\theta = 0.1$) and of both *FS25*
 297 and *FSD25* sharing the same porosity $\theta = 0.25$. The bottom row in Figure 1 displays flow lines (and the
 298 local velocity) within the connected porosity for these three samples and gives a qualitative appraisal of the
 299 dissimilarities between the lowest porosity and the highest porosity samples on one hand, and on the other
 300 hand those occurring between the highest porosity sample of each of the two sets in relation with the pore
 301 network structures. In the following we will quantify these differences and their implications on dispersion.

3.1 Connected porosity geometrical properties retrieved from the BNM

303 As explained in Section 2.1, we computed the Bond Network Model (BNM) for each of the 12 samples,
 304 in order to evaluate the topology and the geometry of the connected porosity and specifically how these
 305 characteristics change with the sample porosity for the *FS* and the *FSD* sets of samples. The main
 306 properties versus porosity are summarized in Figures 2 and 3. The topology of the connected porosity is
 307 characterized by the number of throats (network bonds) and pores (network nodes) per volume of rock
 308 (here the reference is the sample volume) as well as the coordination number κ that denotes the mean
 309 number of throats connected to a given pore. The bonds are characterized by the mean of the radius r_h and
 310 length λ and by the radius r_h distribution displayed in Figure 4.

311 For the *FS* set, decreasing porosity from the highest to the lowest porosity values is obtained by allocating
 312 increasing amounts of cement into localized clusters that acts as increasingly closing connections and thus
 313 decreasing the number of pores and throats and the coordination number. The fixed distribution of the
 314 cement clusters determines the length of the bonds independently of the porosity ($\lambda \approx 65\mu m$), but volume
 315 conservation imposes that the hydraulic radius r_h increases with porosity. The distribution of $r_h/\langle r_h \rangle$ is
 316 wide, decreases almost monotonically from small to high r_h and does not depend on porosity.

317 For the *FSD* set, increasing porosity from the lowest to the highest is obtained by homogeneous erosion
 318 of the solid phase, i.e. both the grains and the cement. The number of pores and throats as well as κ first
 319 decreases for $\theta \leq 0.15$ caused by merging of adjacent throats following a process which is roughly the
 320 opposite of that described for the *FS* set of samples. Then, the number of pores and throats stays almost
 321 constant for $\theta > 0.15$. As a result, the increase of porosity is mainly due to the increase of the throat length
 322 λ and radius r_h . The distribution of $r_h/\langle r_h \rangle$ is almost Gaussian around the mean value, and independent of
 323 the porosity for $\theta > 0.15$. The transition from the original sample *FS10* to the *FSD12* and then *FSD15*
 324 is well visible in the r_h distribution. Note that, as soon as the throats are widely distributed like for the *FS*
 325 set of samples, κ is an indicator of the potential local flow rate disorder at the network nodes because the
 326 probability of having upstream and downstream bonds of distinctly different flow rates is high.

327 Altogether, these results show that the two sets of samples are very different in terms of 1) the topology
 328 of the network; for the *FSD* set, the topology is almost similar for all the porosity range, while it is

329 increasingly complex (with increasing tortuosity, see discussion below) as porosity decreases for the *FS*
 330 set of samples, and 2) the characteristic size of the throats is almost independent of the porosity for the *FD*
 331 set whereas it increases with porosity for the *FSD* set.

332 3.2 Permeability and flow field properties

333 Permeability values k for the 12 samples computed using Darcy's law ($k = \bar{v}_z \mu / \nabla^* p$) are plotted in
 334 the left panel of Figure 5. Permeability increases from $1.4 \times 10^{-13} \text{m}^2$ for sample *SF10* to $6.04 \times 10^{-12} \text{m}^2$
 335 ($6.08 \times 10^{-12} \text{m}^2$) for sample *SF25* (*SFD25*) and are all aligned with the relation $k \sim \theta^4$ independently on
 336 geometrical characteristics of the pore space. The permeability computed on the BNM (solving a Kirchhoff
 337 problem) is also reported Figure 5 in order to evaluate the accuracy of the BNM.

338 The right panel of Figure 5 displays the advective tortuosity χ_a , i.e. the mean tortuosity of the flow
 339 lines. The advective tortuosity is obtained from the ratio of the mean Eulerian speed v_e to the mean
 340 velocity in the direction of the flow v_z (Koponen et al., 1996; Ghanbarian et al., 2014; Puyguiraud et al.,
 341 2019c): $\chi_a = \langle v_e \rangle / \langle v_z \rangle$. For both the samples' sets, χ_a decreases when porosity increases, but it is more
 342 pronounced for the *FS* set of samples. These trends seem to be mainly controlled by the increase of the
 343 throat radius as porosity increases, while the topological characteristic of the network plays a minor role
 344 which is probably resulting from a complex coupling of the geometrical and topologically parameters
 345 discussed above. This makes the advective tortuosity, which is one of the three parameters of the CTRW
 346 model proposed by Puyguiraud et al. (2021), an intrinsic characteristic of the hydrodynamic system that is
 347 essentially porosity-dependant.

348 The distributions of the Eulerian mean speed for the 12 samples are plotted in Figure 6. The dissimilarity
 349 of the $p_m(v)$ curves between the *FS* and the *FSD* sets is clearly visible. The *FSD* samples are displaying
 350 almost the same mean speed distributions with power-law trend $p_m(v) \sim v^{\alpha-1}$ for $v < \langle v_m \rangle$ with
 351 $\alpha = 0.245 \pm 0.05$. For the *FS* set, the evolution of $p_m(v)$ with porosity includes two features. First, $p_m(v)$
 352 gradually diverges from a Gamma distribution as porosity increases, with the occurrence of increasingly
 353 marked transition between the values of speed larger than the mean ($v > \langle v_m \rangle$) and the power-law slope
 354 for the slower speed values. Second, the power-law slope for $v \ll \langle v_m \rangle$ increases when porosity decreases,
 355 ranging from $\beta = \alpha - 1 = 1.63$ for $\theta = 0.25$ to $\beta = 1.75$ for $\theta = 0.10$. These values are in agreement
 356 with the value of 1.65 found by Puyguiraud et al. (2021) for the Beara sandstone. As far as we know,
 357 they have been very few studies of the correlation between the flow speed distribution and the properties of
 358 the pore space microstructures (Siena et al., 2014; Matyka et al., 2016; Alim et al., 2017). For instance,
 359 Alim et al. (2017) investigated this issue using numerical simulations in 2-dimensional simple artificial
 360 porous media made of circular or elliptical discs placed on a square or triangular lattices with increasing
 361 disorder. By extracting and analyzing the corresponding network of tubes, following a procedure quite
 362 similar to that implemented for extracting the BNM (Section 2.4), they concluded that the flow distribution
 363 is mainly determined by the distribution of fractions of fluid flowing at each of the network node and not by
 364 the overall tube size distribution. Our results lead us to a similar conclusion for the complex 3-dimensional
 365 porous media studied here. The evolution of the mean flow speed with porosity for the *FS* set in comparison
 366 with the weak evolution of the mean flow speed with porosity for the *FSD* set appears to be correlated to
 367 the noticeable increase with porosity of the number of throats as well as the mean number of throats per
 368 pore κ (Figure 3) measured for the *FS* set, whereas both the number of throats and κ are almost constant
 369 for the *FSD* set of samples.

370 3.3 Speed decorrelation distance length

371 The decorrelation distance ℓ_c is evaluated from the Lagrangian flux weighted speed autocorrelation
 372 function $\Upsilon_{vv}(l) = \langle (v_v(s) - \langle v_v \rangle)(v_v(s+l) - \langle v_v \rangle) \rangle / \sigma_{v_v}^2$, where l denotes the lag. The decorrelation

373 distance ℓ_c is given by the value of the lag corresponding to $\Upsilon_{vv}(l) = 1/e$. The two panels at left of
 374 Figure 7 display the Lagrangian flux weighted speed autocorrelation function $\Upsilon_{vv}(l)$ for the two set of
 375 samples. The corresponding values of the decorrelation distance ℓ_c versus porosity are given in the third
 376 panel of Figure 7, and the ratio of the decorrelation distance to the mean throat length $\eta = \ell_c/\lambda$ versus
 377 porosity is given in the right panel.

378 For both the sample sets, the decorrelation distance ℓ_c increases with porosity from about $150 \mu\text{m}$ at
 379 $\theta = 0.1$ to about $240 \mu\text{m}$ for *FS* and $290 \mu\text{m}$ for *FSD*. The slight increase of ℓ_c for the *FSD* set for
 380 $\theta > 0.15$ compared to the *FS* set is caused by the increase of the throat radius and the decrease of tortuosity
 381 with porosity that are more important for *FSD* than for *FS*. The ratio η also displays an increase with
 382 porosity following a similar trend for both the *FS* and the *FSD* set of samples, the values for *FSD* being
 383 smaller of ~ 0.5 unit than for *FS*. Thus, in average, the number of bond lengths travelled before losing the
 384 memory of the initial speed ranges from about 2 to 4. These values are in good agreement with the value of
 385 4 obtained by Puyguiraud et al. (2021) by fitting DNS and CTRW for Berea sandstone of porosity 0.18.

386 3.4 Dispersion

387 In this section we are presenting the results of the transport DNS, discussing them in the frame of
 388 the scaling properties derived from the CTRW model proposed by Puyguiraud et al. (2021) and of the
 389 properties retrieved from the BNM (Section 3.1).

390 The first passage time distributions $f_t(t)$ (or breakthrough curves) at a distance of 20 times the sample
 391 size are given in Figure 8 for $Pe = 100$ and also for purely advective transport ($d_m = 0; Pe = \infty$).
 392 For the latter, all the curves display the power-law tailing that characterize pre-asymptotic (non-Fickian)
 393 regime over 3 to 4 orders of magnitude. The scaling $f_t(t) \sim t^{-2-\alpha}$ predicted by Puyguiraud et al. (2021)
 394 with the values of α corresponding to those measured on the mean speed distribution is confirmed for
 395 all the samples. The comparison of the value of α ($0.24 \leq \alpha \leq 0.37$) for the *FS* set of samples is given
 396 in Figure 9. For $Pe = 100$, even if it can be considered a quite large value for natural porous media,
 397 diffusion acts as increasing the rate at which $f_t(t)$ decreases with time and the α -dependent power-law
 398 trend is not present. Note that the beginning of the exponential decrease is visible for *FSD25* at $t \approx 5\tau_D$,
 399 where $\tau_D = \ell_c^2/d_m \approx 80\text{s}$.

400 We now focus on determining the asymptotic dispersion coefficient D^* from the asymptotic regime of
 401 the displacement variance. Figure 10 displays, as an example, the displacement variance normalized to
 402 the throat length (σ^2/λ^2) for the 12 samples in the case $Pe = 100$, but the following comments apply for
 403 all values of Pe larger than 1. All curves converge to the asymptotic regime ($\sigma^2/\lambda^2 \sim t$) for time $t \geq t_a$,
 404 where t_a is independent of the value of Pe but depends on porosity; $t_a \approx 10^3\text{s}$ for $\theta = 0.1$ and $t_a \approx 10^4\text{s}$
 405 for $\theta = 0.25$, i.e. about 40 and 120 times τ_D , respectively. This point is important regarding the possibilities
 406 of measuring the asymptotic dispersion from laboratory experiments, deriving D^* from the breakthrough
 407 curves, for instance. For $Pe = 100$, that corresponds to a mean flow speed of $1.5 \times 10^{-3} \text{ m/s}$ for *FS10*, a
 408 sample of about 1.5 m long displaying the same properties of the mm-scale sample would be necessary
 409 to measure D^* ; a distance of 60 m would be necessary for $Pe = 4000$. This indicates that experimental
 410 measurement of D^* can be performed only for low values of Pe , typically of the order $Pe \leq 10$. However,
 411 for such low values of Pe it is not possible to measure α and thus determine the trend $D^*(Pe)$.

412 Conversely, the DNS allows us to perform numerical experiments over large range of Pe values; Figure 11
 413 displays the value of D^* versus Pe for the 12 samples from diffusion-dominant regime ($Pe = 10^{-3}$)
 414 to advection-dominant ($Pe = 2 \times 10^4$). These curves can be commented in terms of their slope and of
 415 their scaling with porosity, for $Pe \gg 1$. Note that for $Pe \rightarrow 0$ the ratio D^*/d_m is equal to the inverse

416 of the diffusive tortuosity ($D^*/d_m = \chi_d^{-1}$). For both the *FS* and *FSD* sets of samples, the relation
 417 $D^*/d_m \propto Pe^{2-\alpha}$ predicted by the CTRW model for $Pe \gg 1$ is observed. The values of α compared to
 418 those measured using the speed distribution and the tailing of $f_t(t)$ are given in Figure 9. The minimum
 419 value Pe_c at which $D^*/d_m \propto Pe^{2-\alpha}$ is effectively observed, is correlated with the shape of the mean speed
 420 distribution (Figure 6). For *FS10*, the trend $p_m(v) \sim v^{\alpha-1}$ with $\alpha = 0.24$ extends up to $5 \times 10^{-3}v/\langle v_m \rangle$,
 421 while for *FS25* the trend $\alpha = 0.37$ extends up to $3 \times 10^{-4}v/\langle v_m \rangle$ only. This gives values of Pe_c ranging
 422 from 1000 for *FS10* to 50 for *FS25*. The same trend is observed for the *FSD* set of samples. These results
 423 demonstrate the clear control of the particle mean speed distribution on the evolution of D^* with the Péclet
 424 number. However, both the two sets of samples display a scaling of D^* with porosity, independently of
 425 the slope determined for $Pe \geq Pe_c$. The expected decrease of D^* for all values of $Pe > 1$ when porosity
 426 increases, corresponding to a decrease of the slope of $p_m(v)$ for $v \ll \langle v_m \rangle$ is clearly visible for the *FS*
 427 set of samples. But, the results for the *FSD* set, that share the same mean speed distribution (Figure 6),
 428 show also a clear decrease of D^* as porosity increases, which indicates that the dispersion scaling with
 429 porosity is not solely controlled by $p_m(v)$ for $v \ll \langle v_m \rangle$. Indeed, the increase of D^* with porosity is also
 430 related to the increase of the speed decorrelation distance ℓ_c with porosity. In the frame of the CTRW
 431 model ℓ_c denotes the length at which a new velocity is drawn from the mean speed distribution, and as such
 432 ℓ_c determines the rate at which the speed changes.

433 Furthermore, we observe in Figure 11 that D^* shows different power-law behaviors for $Pe < Pe_c$ that
 434 can be related to the scaling behavior of the distribution of mean flow speeds and the transition time
 435 distribution. In the limit of infinite Pe , the transition time distribution is given by (12). For finite Pe , it
 436 is cut-off at the diffusion time τ_D . The log-slope of $\psi(t)$ at the cut-off time depends on the average flow
 437 speed $\langle v_m \rangle$. This is shown in Figure 12, which displays the distribution of purely advective transition
 438 times rescaled by $\tau_v = \ell_c/\langle v_m \rangle$ for *FS10* and *FS25*. The behavior of D^* for $Pe < Pe_c$ corresponds to
 439 the power-law scaling of $\psi(t)$ at dimensionless times equal to Pe . The slope of the $\psi(t)$ curves display
 440 the power-law behaviors $t^{-2-\alpha'}$ for $Pe < Pe_c$ with $\alpha' = 0.38$ and 0.79 for *FS10* and *FS25*, respectively.
 441 For $Pe \geq Pe_c$ the values of α are similar to those reported in Figure 9 for $f_t(t)$, $p_m(v)$ and $D^*(Pe)$, i.e.
 442 $\alpha = 0.23$ and 0.37 for *FS10* and *FS25*, respectively.

4 SUMMARY AND CONCLUSIONS

443 We performed numerical experiments of passive solute transport for two sets of porous media mimicking a
 444 large range of porosity and microstructures expected in sandstones. The aim was to test the validity of the
 445 CTRW model, to explore how the flow field characteristics are linked to the porous media geometrical
 446 properties and to determine the scaling of asymptotic dispersion coefficient D^* with the Péclet number. The
 447 two sets of six samples share similar porosity, ranging from 0.1 to 0.25, and the same permeability-porosity
 448 trend $k(\theta)$ but displays distinctly different microstructures and thus dispersion evolution.

449 The conceptual CTRW model of solute transport in porous media, as the one proposed by Puyguiraud
 450 et al. (2021), infers that solute spreading along particle paths is controlled by the transition time of the
 451 solute particles which is determined by the distribution of solute particle mean speeds $p_m(v)$, the velocity
 452 decorrelation distance ℓ_c and diffusion. The effective tortuosity factor that depends on Pe and on the
 453 advective tortuosity χ_a (that can be also easily evaluated from the flow field) allows mapping dispersion
 454 in the streamwise direction which is aligned with the mean pressure gradient. With decreasing Pe , the
 455 effective tortuosity of the solute particles increases and the control of $p_m(v)$ on dispersion decreases
 456 but remains important up to high values of Pe because of the wide distribution of the particles speeds

457 toward low speed values. This means that for heterogeneous media, such as sandstones, the pre-asymptotic
 458 (non-Fickian) dispersion regime is likely to persist over long time scales.

459 We found that the scaling properties, measured by the coefficient α , predicted by Puyguiraud et al.
 460 (2021)'s model are effectively measurable for all the 12 studied samples. For instance, results shows
 461 that at high Pe , the tail of the breakthrough curves, that is controlled by the low flow speeds, scales as
 462 $f_t(t) \sim t^{-2-\alpha}$ where α is given by the slope of the mean speed distribution $p_m(v) \sim v^{\alpha-1}$, for $v < \langle v_m \rangle$.
 463 As Pe decreases, diffusion eventually dominates over low flow speeds, thus cuts off the power-law tail of
 464 the breakthrough curves and leads to Fickian behavior from which the asymptotic dispersion coefficient
 465 D^* can be theoretically evaluated (Van Genuchten and Wierenga, 1986). However, the analysis of the
 466 displacement variance $\sigma^2(t)$ indicates that D^* cannot be measured experimentally at laboratory scale, for
 467 high values of Pe , because the distance required for reaching the asymptotic regime is orders of magnitude
 468 larger than what is workable at laboratory scale. Thus, measuring experimentally the value of α , for
 469 determining how D^* scales with Pe seems difficult.

470 The asymptotic dispersion coefficient D^* was computed up to the largest values of Pe expected for
 471 laminar flow in natural environments. Results show that $D^*/d_m \propto Pe^{2-\alpha}$ from Pe_c up to the highest
 472 value of Pe ($Pe = 4000$). Note that for the values of α expected for such heterogeneous rock samples,
 473 neither the trend $D^* \sim Pe \ln(Pe)$ (Saffman, 1959; Koch and Brady, 1985) assuming that the distribution
 474 of flow speeds is flat ($\alpha = 1$), nor the trend $D^* \sim Pe$ expected for $\alpha > 1$ at high Pe are expected. For
 475 $1 < Pe < Pe_c$, $D^*/d_m \propto Pe^{2-\alpha'}$ where $\alpha' > \alpha$ depends on the mean speed distribution and the speed
 476 decorrelation distance ℓ_c that are the parameters that determine the advective particle transition distribution
 477 and subsequently the value of Pe_c . The mean particle speed remains correlated for longer distances in
 478 porous media with straighter and larger bonds (throats). As such ℓ_c is a good indicator of the complexity
 479 of flow field, because it encompasses the effect of tortuosity that ubiquitously decreases with increasing
 480 porosity and the effect of the mean throat radius that ubiquitously increases with porosity, while the other
 481 structural parameters are distinctly different for the two sets of samples. Yet, when reported in term of
 482 number of bonds length travelled before speed decorrelates, it is observed that FS and FSD sets behave
 483 quite similarly; the equivalent number of pores (intersection nodes) crossed before losing the memory of
 484 the initial speed equals $\eta - 1$ and ranges from about 1 for $\theta = 0.1$ to about 3 for $\theta = 0.25$. We conjecture
 485 that the increase of the number nodes crossed before speed decorrelates is linked to the speed changes
 486 caused by the splitting of the flow at the network node and thus to both the mean radius of the bonds and
 487 the coordination number κ . Similar conjecture can be done for the distribution of the solute mean speed
 488 $p_m(v)$ which should be controlled by the speed changes caused by splitting of the flow where throats are
 489 connected, as it was anticipated by Alim et al. (2017) in numerical simulations in 2-dimensional simple
 490 artificial networks. The structural and hydrodynamic mechanisms that determine the flow distribution
 491 in 3-dimensional porous media, focusing on the impact pore size distribution, coordination number and
 492 local correlations on the speed distributions will be discussed in a forthcoming paper. Yet, from the results
 493 presented in this paper, one can conclude that the flow distribution, and thus the mean speed, are controlled
 494 by the distribution of fractions of fluid flowing at each of the network nodes which in turn is determined
 495 by the distribution of the throat radius (and not the mean) and the coordination number. At given porosity
 496 and mean bond radius the latter is controlled by the number of throats per unit volume that increases with
 497 porosity for the FS set and decrease with porosity for the FSD set of samples. We believe that these results
 498 give a first insight into both the mechanisms and the microstructural parameters that control dispersion in
 499 porous media.

ACKNOWLEDGMENTS

REFERENCES

- 500 Alim, K., Parsa, S., Weitz, D. A., and Brenner, M. P. (2017). Local pore size correlations determine flow
 501 distributions in porous media. *Phys. Rev. Lett.* 119, 144501. doi:10.1103/PhysRevLett.119.144501
- 502 Bear, J. (1972). *Dynamics of fluids in porous media* (American Elsevier, New York)
- 503 [Dataset] Berg, C. F. (2016a). Fontainebleau 3d models. [http://www.digitalrockportal.](http://www.digitalrockportal.org/projects/57)
 504 [org/projects/57](http://www.digitalrockportal.org/projects/57). doi:doi:10.17612/P75P4P
- 505 Berg, C. F. (2016b). Fundamental transport property relations in porous media incorporating detailed pore
 506 structure description. *Transport in porous media* 112, 467–487
- 507 Bijeljic, B. and Blunt, M. J. (2006). Pore-scale modeling and continuous time random walk analysis of
 508 dispersion in porous media. *Water Resources Research* 42. doi:https://doi.org/10.1029/2005WR004578
- 509 Bijeljic, B. and Blunt, M. J. (2007). Pore-scale modeling of transverse dispersion in porous media. *Water*
 510 *Resources Research* 43. doi:https://doi.org/10.1029/2006WR005700
- 511 Bijeljic, B., Mostaghimi, P., and Blunt, M. J. (2011). Signature of non-Fickian solute transport in complex
 512 heterogeneous porous media. *Phys. Rev. Lett.* 107, 204502
- 513 Bijeljic, B., Muggeridge, A. H., and Blunt, M. J. (2004). Pore-scale modeling of longitudinal dispersion.
 514 *Water Resources Research* 40
- 515 Bijeljic, B., Raeini, A., Mostaghimi, P., and Blunt, M. J. (2013). Predictions of non-fickian solute transport
 516 in different classes of porous media using direct simulation on pore-scale images. *Physical Review E* 87.
 517 doi:10.1103/physreve.87.013011
- 518 Brenner, H. and Edwards, D. (1993). *Macrotransport Processes* (Butterworth-Heinemann, MA, USA)
- 519 Carrel, M., Morales, V. L., Dentz, M., Derlon, N., Morgenroth, E., and Holzner, M. (2018). Pore-scale
 520 hydrodynamics in a progressively bioclogged three-dimensional porous medium: 3-d particle tracking
 521 experiments and stochastic transport modeling. *Water resources research* 54, 2183–2198
- 522 Chatzis, I. and Dullien, F. A. (1985). The modeling of mercury porosimetry and the relative permeability
 523 of mercury in sandstones using percolation theory. *Int. Chem. Eng.; (United States)* 25
- 524 Danckwerts, P. (1953). Continuous flow systems: Distribution of residence times. *Chemical Engineering*
 525 *Science* 2, 1–13. doi:https://doi.org/10.1016/0009-2509(53)80001-1
- 526 De Anna, P., Le Borgne, T., Dentz, M., Tartakovsky, A. M., Bolster, D., and Davy, P. (2013). Flow
 527 intermittency, dispersion, and correlated continuous time random walks in porous media. *Physical*
 528 *review letters* 110, 184502
- 529 Delay, F., Ackerer, P., and Danquigny, C. (2005). Simulating solute transport in porous or fractured
 530 formations using random walk particle tracking. *Vadose Zone J.* 4, 360–379
- 531 Delgado, J. M. P. Q. (2006). A critical review of dispersion in packed beds. *Heat and Mass Transfer* 42,
 532 279–310
- 533 Dentz, M. (2012). Concentration statistics for transport in heterogeneous media due to stochastic
 534 fluctuations of the center of mass velocity. *Advances in Water Resources* 36, 11–22. doi:10.1016/j.
 535 [advwatres.2011.04.005](https://doi.org/10.1016/j.advwatres.2011.04.005)
- 536 Dentz, M., Borgne, T. L., Englert, A., and Bijeljic, B. (2011). Mixing, spreading and reaction in
 537 heterogeneous media: A brief review. *Journal of Contaminant Hydrology* 120-121, 1 – 17. doi:
 538 <https://doi.org/10.1016/j.jconhyd.2010.05.002>. Reactive Transport in the Subsurface: Mixing, Spreading
 539 and Reaction in Heterogeneous Media
- 540 Dentz, M., Icardi, M., and Hidalgo, J. J. (2018). Mechanisms of dispersion in a porous medium. *Journal of*
 541 *Fluid Mechanics* 841, 851–882. doi:10.1017/jfm.2018.120
- 542 Fischer, H. B. (1966). *Longitudinal dispersion in laboratory and natural streams: Report No. KH-R -12.*
 543 Tech. rep., California Inst. of Technology

- 544 Ghanbarian, B., Hunt, A. G., Ewing, R. P., and Skinner, T. E. (2014). Universal scaling of the formation
545 factor in porous media derived by combining percolation and effective medium theories. *Geophysical*
546 *Research Letters* 41, 3884–3890. doi:10.1002/2014GL060180
- 547 Gjetvaj, F., Russian, A., Gouze, P., and Dentz, M. (2015). Dual control of flow field heterogeneity
548 and immobile porosity on non-fickian transport in berea sandstone. *Water Resources Research* 51,
549 8273–8293. doi:10.1002/2015WR017645
- 550 Gouze, P., Borgne, T. L., Leprovost, R., Lods, G., Poidras, T., and Pezard, P. (2008). Non-fickian dispersion
551 in porous media: 1. Multiscale measurements using single-well injection withdrawal tracer tests. *Water*
552 *Resources Research* 44. Doi:10.1029/2007WR006278
- 553 Gouze, P., Puyguiraud, A., Roubinet, D., and Dentz, M. (2021). Pore-scale transport in rocks of different
554 complexity modeled by random walk methods. *Transport in Porous Media* , 1573–1634doi:10.1007/
555 s11242-021-01675-2
- 556 Guibert, R., Horgue, P., Debenest, G., and Quintard, M. (2016). A comparison of various methods for the
557 numerical evaluation of porous media permeability tensors from pore-scale geometry. *Mathematical*
558 *Geosciences* 48, 329–347
- 559 Han, N.-W., Bhakta, J., and Carbonell, R. G. (1985). Longitudinal and lateral dispersion in packed
560 beds: Effect of column length and particle size distribution. *AICHE Journal* 31, 277–288. doi:https:
561 //doi.org/10.1002/aic.690310215
- 562 Icardi, M., Boccardo, G., Marchisio, D. L., Tosco, T., and Sethi, R. (2014). Pore-scale simulation of fluid
563 flow and solute dispersion in three-dimensional porous media. *Physical Review E* 90, 013032
- 564 Kang, P. K., de Anna, P., Nunes, J. P., Bijeljic, B., Blunt, M. J., and Juanes, R. (2014). Pore-scale
565 intermittent velocity structure underpinning anomalous transport through 3-d porous media. *Geophysical*
566 *Research Letters* 41, 6184–6190. doi:10.1002/2014GL061475
- 567 Kinzel, D. L. and Hill, G. A. (1989). Experimental study of dispersion in a consolidated sandstone. *The*
568 *Canadian Journal of Chemical Engineering* 67, 39–44. doi:https://doi.org/10.1002/cjce.5450670107
- 569 Koch, D. L. and Brady, J. F. (1985). Dispersion in fixed beds. *Journal of Fluid Mechanics* 154, 399–427.
570 doi:10.1017/s0022112085001598
- 571 Koponen, A., Kataja, M., and Timonen, J. (1996). Tortuous flow in porous media. *Physical Review E* 54,
572 406
- 573 Lee, T., Kashyap, R., and Chu, C. (1994). Building skeleton models via 3-d medial surface axis thinning
574 algorithms. *CVGIP: Graphical Models and Image Processing* 56, 462–478. doi:https://doi.org/10.1006/
575 cgip.1994.1042
- 576 Levy, M. and Berkowitz, B. (2003). Measurement and analysis of non-Fickian dispersion in heterogeneous
577 porous media. *Journal of contaminant hydrology* 64, 203–226
- 578 Li, M., Qi, T., Bernabé, Y., Zhao, J., Wang, Y., Wang, D., et al. (2018). Simulation of solute transport
579 through heterogeneous networks: analysis using the method of moments and the statistics of local
580 transport characteristics. *Scientific Reports* 8. doi:10.1038/s41598-018-22224-w
- 581 Matyka, M., Gołembiewski, J., and Koza, Z. (2016). Power-exponential velocity distributions in disordered
582 porous media. *Phys. Rev. E* 93, 013110. doi:10.1103/PhysRevE.93.013110
- 583 Morales, V. L., Dentz, M., Willmann, M., and Holzner, M. (2017). Stochastic dynamics of intermittent
584 pore-scale particle motion in three-dimensional porous media: Experiments and theory. *Geophysical*
585 *Research Letters* 44, 9361–9371
- 586 Moroni, M. and Cushman, J. H. (2001). Statistical mechanics with three-dimensional particle tracking
587 velocimetry experiments in the study of anomalous dispersion. II. experiments. *Physics of Fluids* 13,
588 81–91. doi:10.1063/1.1328076

- 589 Oren, P.-E. (2002). Process based reconstruction of sandstones and prediction of transport properties.
 590 *Transport in porous media* 46, 311–343
- 591 Pfannkuch, H. O. (1963). Contribution a l'étude des déplacements de fluides miscibles dans un milieu
 592 poreux. *Rev. Inst. Fr. Petr.* 18, 215–270
- 593 Puyguiraud, A., Gouze, P., and Dentz, M. (2019a). Is there a representative elementary volume for
 594 anomalous dispersion? *Transport in Porous Media* doi:10.1007/s11242-019-01366-z
- 595 Puyguiraud, A., Gouze, P., and Dentz, M. (2019b). Stochastic dynamics of lagrangian pore-scale velocities
 596 in three-dimensional porous media. *Water Resources Research* 55. doi:10.1029/2018WR023702
- 597 Puyguiraud, A., Gouze, P., and Dentz, M. (2019c). Upscaling of anomalous pore-scale dispersion.
 598 *Transport in Porous Media*
- 599 Puyguiraud, A., Gouze, P., and Dentz, M. (2021). Pore-scale mixing and the evolution of hydrodynamic
 600 dispersion in porous media. *Phys. Rev. Lett.* 126, 164501. doi:10.1103/PhysRevLett.126.164501
- 601 Russian, A., Dentz, M., and Gouze, P. (2016). Time domain random walks for hydrodynamic transport in
 602 heterogeneous media. *Water Resources Research* 52, 3309–3323. doi:10.1002/2015WR018511
- 603 Saffman, P. G. (1959). A theory of dispersion in a porous medium. *Journal of Fluid Mechanics* 6, 321–349
- 604 Sahimi, M. (2011). *Flow and transport in porous media and fractured rock: from classical methods to*
 605 *modern approaches* (John Wiley & Sons)
- 606 Sahimi, M., Hughes, B. D., Scriven, L., and Davis, H. T. (1986). Dispersion in flow through porous
 607 media—i. one-phase flow. *Chemical engineering science* 41, 2103–2122
- 608 Sahimi, M. and Imdakm, A. (1988). The effect of morphological disorder on hydrodynamic dispersion in
 609 flow through porous media. *Journal of Physics A* 21, 3833–3870
- 610 Seymour, J. D. and Callaghan, P. T. (1997). Generalized approach to nmr analysis of flow and dispersion
 611 in porous media. *AIChE Journal* 43, 2096–2111. doi:https://doi.org/10.1002/aic.690430817
- 612 Seymour, J. D., Gage, J. P., Codd, S. L., and Gerlach, R. (2004). Anomalous fluid transport in porous
 613 media induced by biofilm growth. *Physical Review Letters* 93. doi:10.1103/physrevlett.93.198103
- 614 Siddiqi, K. and Pizer, S. (2008). *Medial Representations: Mathematics, Algorithms and Applications*
 615 (Springer Publishing Company, Incorporated), 1st edn.
- 616 Siena, M., Riva, M., Hyman, J. D., Winter, C. L., and Guadagnini, A. (2014). Relationship between pore
 617 size and velocity probability distributions in stochastically generated porous media. *Phys. Rev. E* 89,
 618 013018. doi:10.1103/PhysRevE.89.013018
- 619 Souzy, M., Lhuissier, H., Méheust, Y., Borgne, T. L., and Metzger, B. (2020). Velocity distributions,
 620 dispersion and stretching in three-dimensional porous media. *Journal of Fluid Mechanics* 891. doi:10.
 621 1017/jfm.2020.113
- 622 Taylor, G. (1953). Dispersion of soluble matter in solvent flowing slowly through a tube. In *Proceedings of*
 623 *the Royal Society of London A: Mathematical, Physical and Engineering Sciences* (The Royal Society),
 624 vol. 219, 186–203
- 625 Van Genuchten, M. T. and Wierenga, P. J. (1986). *Solute Dispersion Coefficients and Retardation Factors*
 626 (John Wiley Sons, Ltd), chap. 44. 1025–1054. doi:https://doi.org/10.2136/sssabookser5.1.2ed.c44
- 627 Weller, H. G., Tabor, G., Jasak, H., and Fureby, C. (1998). A tensorial approach to computational continuum
 628 mechanics using object-oriented techniques. *Computers in physics* 12, 620–631
- 629 Whitaker, S. (1967). Diffusion and dispersion in porous media. *AIChE Journal* 13, 420–427. doi:https:
 630 //doi.org/10.1002/aic.690130308

FIGURE CAPTIONS

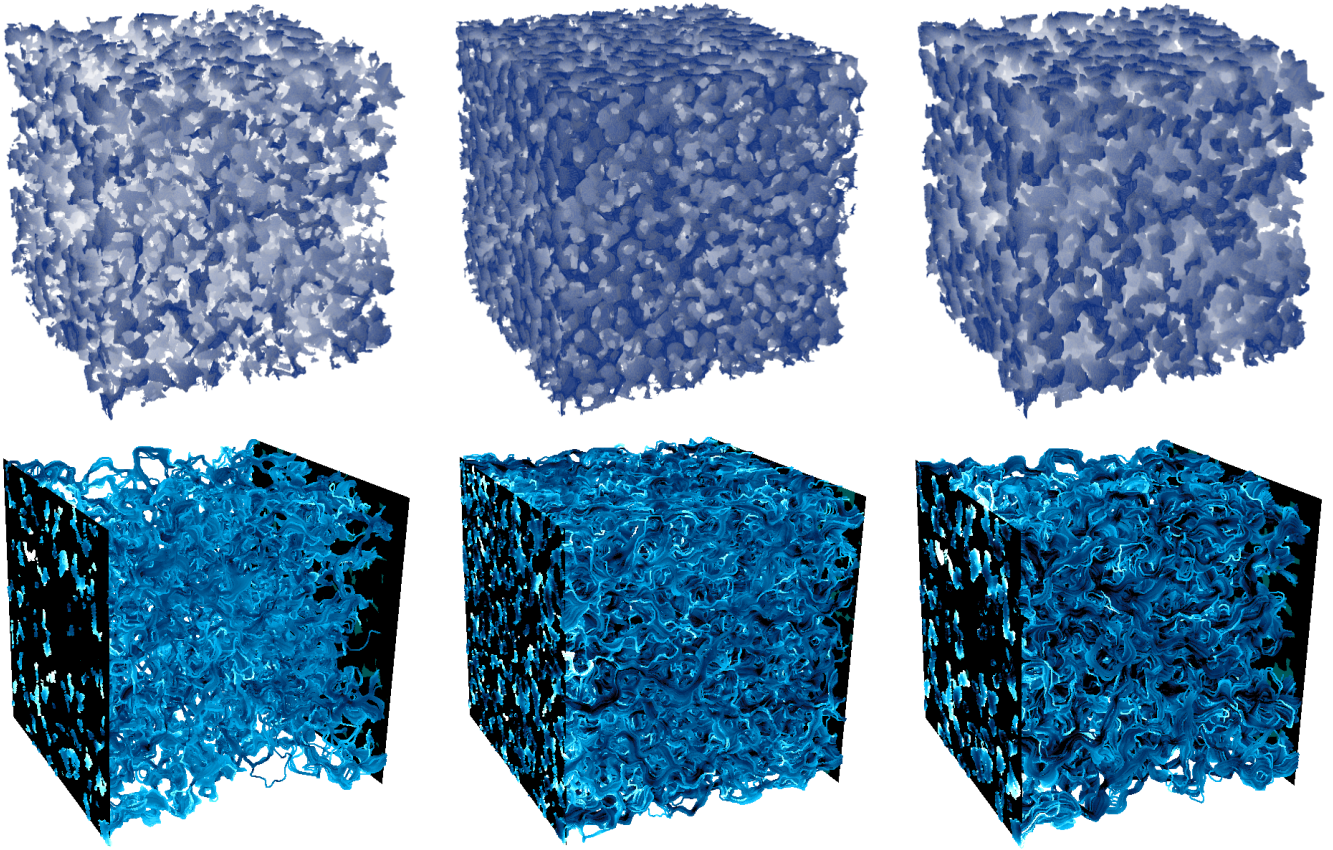


Figure 1. Three-dimensional structure of *FS10* (left), *FS25* (middle), *FSD25* (right) samples. The top row displays the void space. The lines in the bottom panel show particle paths, the color scheme indicating the particle speed from white ($u/\langle u \rangle \leq 7 \times 10^{-4}$) to dark blue ($u/\langle u \rangle = 10$).

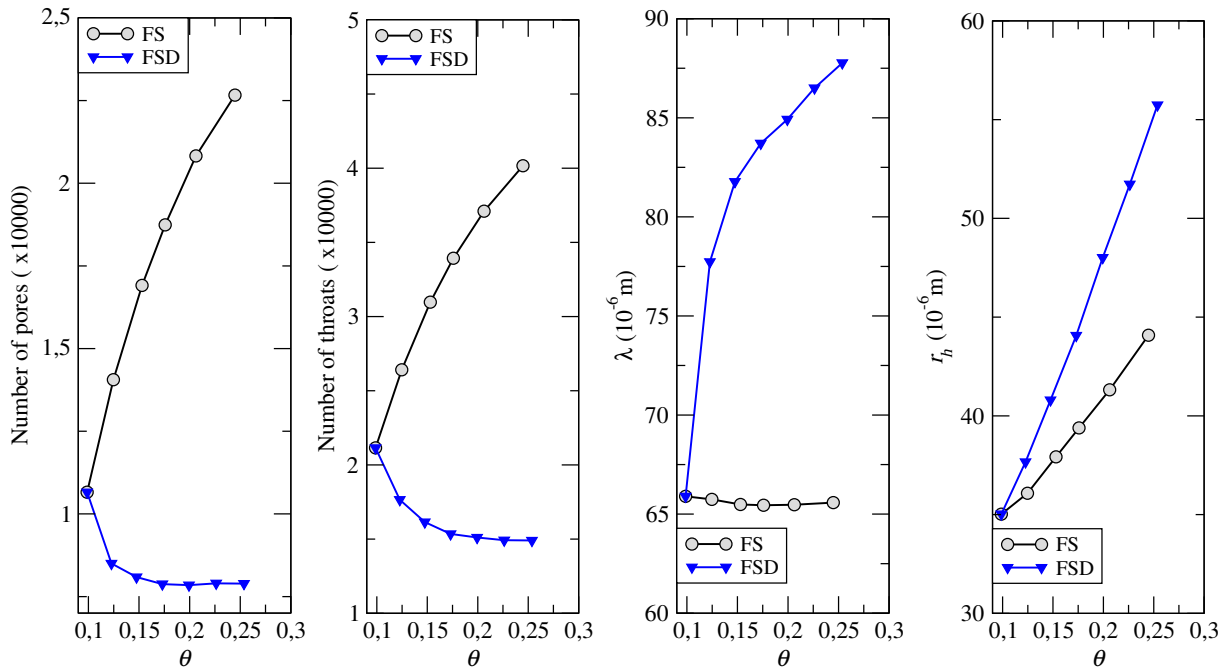


Figure 2. From left to right panels: number of pores; number of throats; mean throat length λ ; mean throat radius r_h versus porosity θ for the *FS* and *FSD* samples.

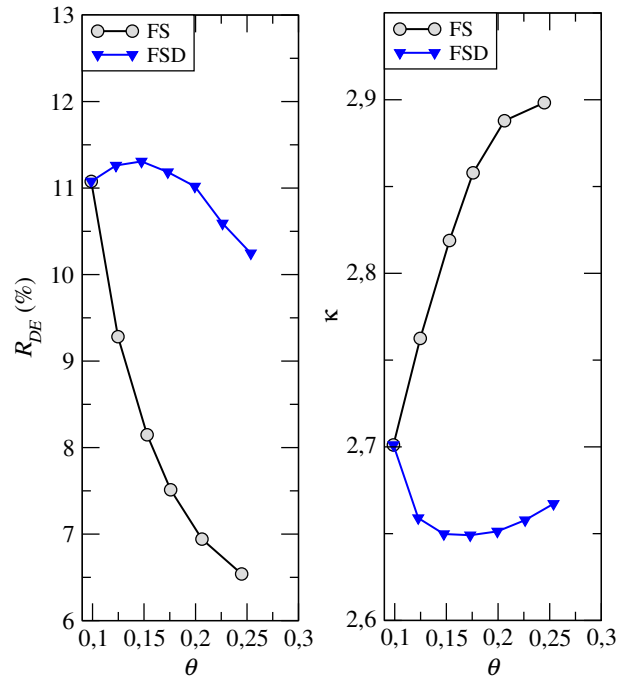


Figure 3. Left, ratio (in %) of the number of dead-ends to the number of throats; right, mean number of throats per pore κ versus porosity θ for the *FS* and *FSD* samples.

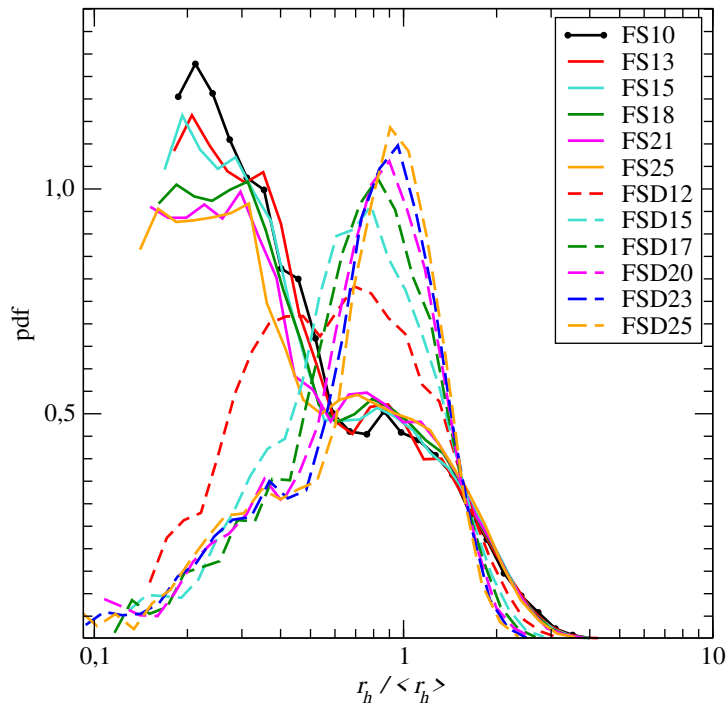


Figure 4. Normalized distribution of r_h for the *FS* and *FSD* samples.

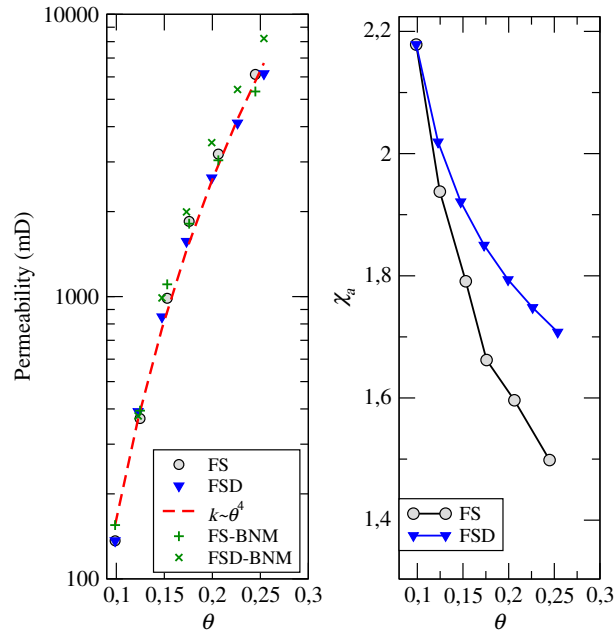


Figure 5. Permeability (left panel) and advective tortuosity χ_a (right panel) versus porosity θ for the *FS* and *FSD* samples.

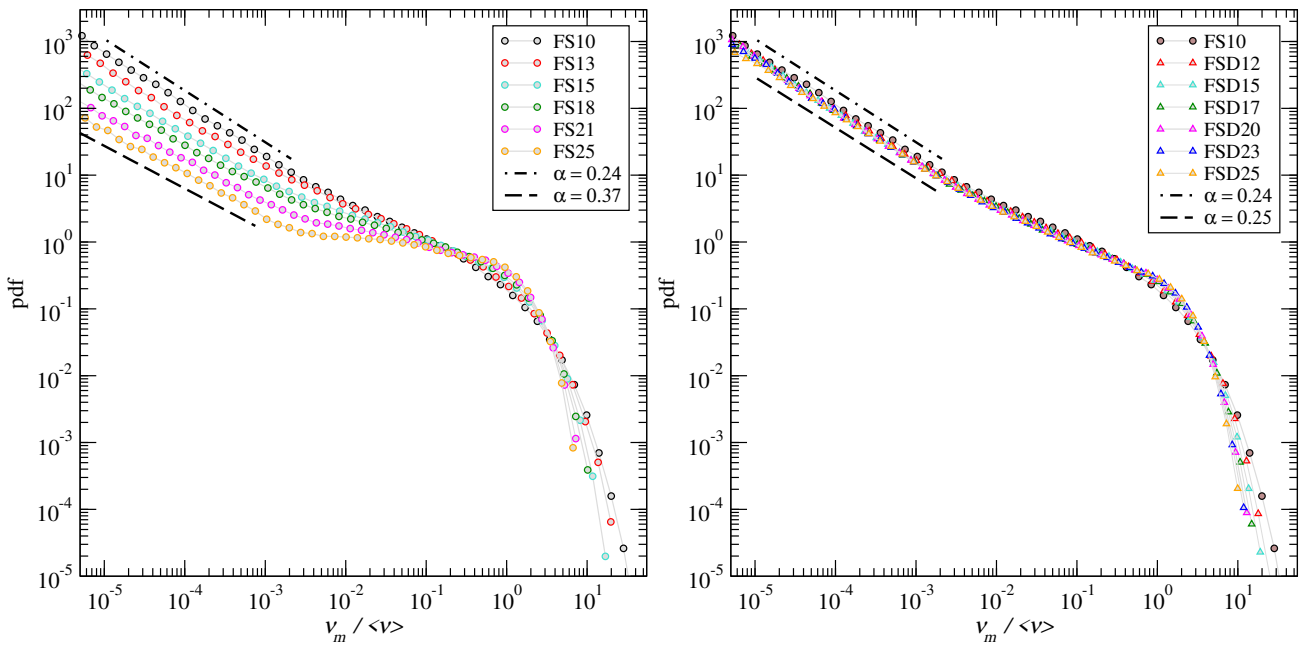


Figure 6. Distribution of the Eulerian mean speeds $p_m(v)$ normalized to its mean, for the *FS* (left panel) and the *FSD* (right panel) samples.

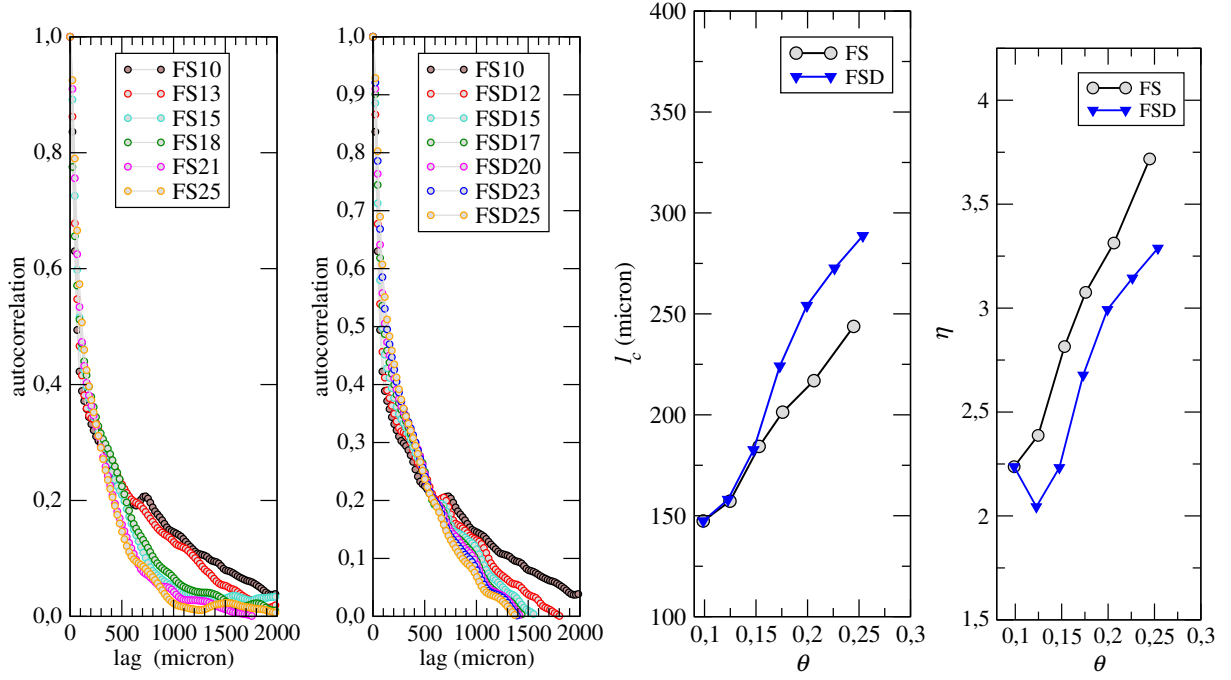


Figure 7. Flux weighted Langrangian speed auto-correlation function $\Upsilon_{v_v}(l)$ for the *FS* (left panel) and the *FSD* (middle-left panel) samples. The middle-right panel displays the decorrelation length l_c and the right panel displays the ratio $\eta = l_c/\lambda$ versus porosity.

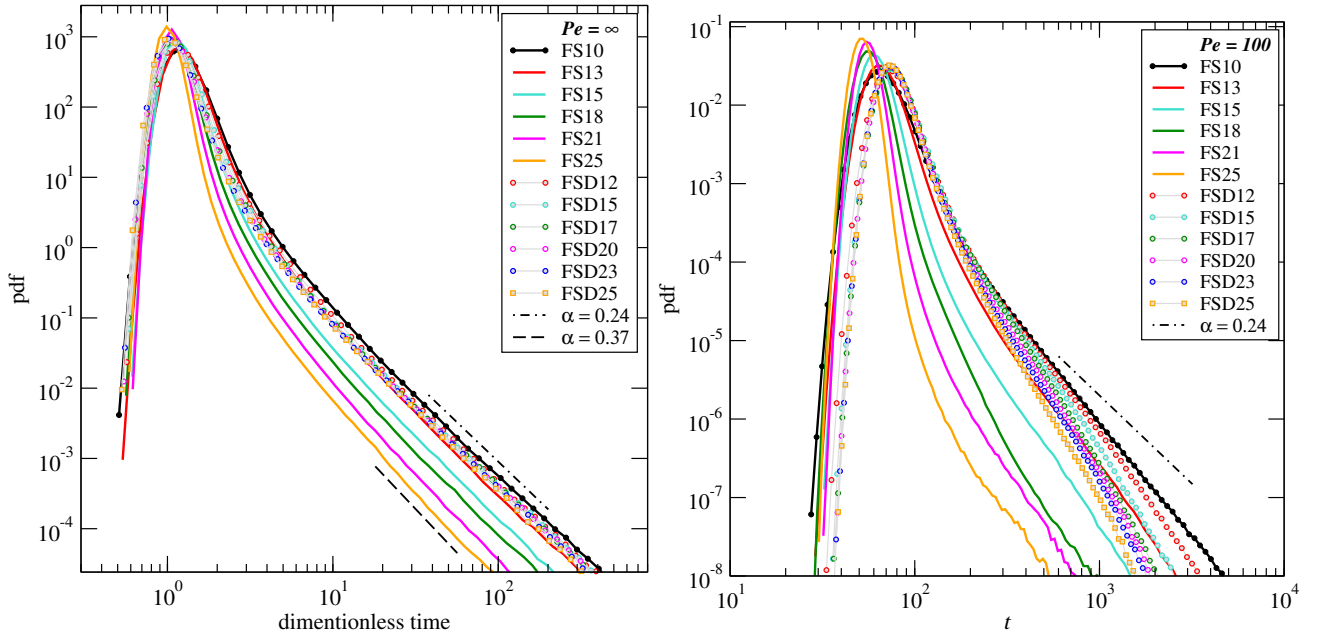


Figure 8. First passage time PDF f_t at $Z = 5.47 \times 10^{-2}$ m from the inlet. Left: results for infinite Pe versus dimensionless time Z/v . Right: results for $Pe = 100$ versus time.

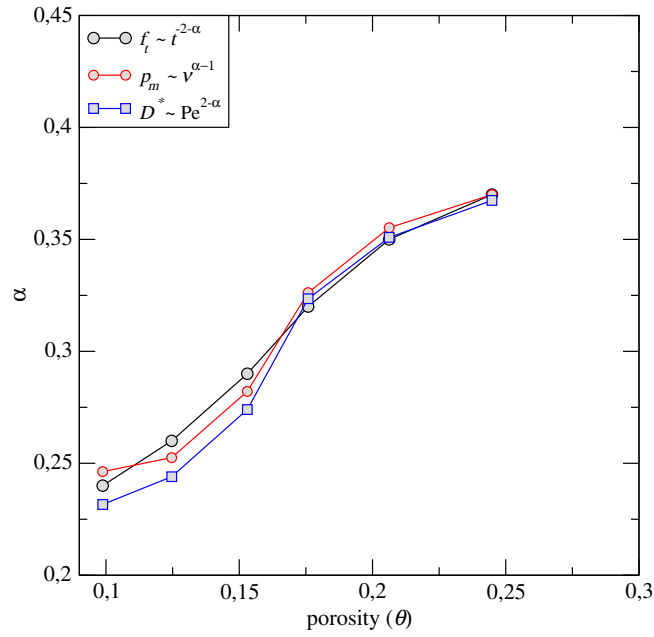


Figure 9. Comparison of the value of α for the *FS* samples evaluated from 1) the slope of the first passage time plotted in the left panel, 2) the slope of the mean speed PDF plotted in Figure 6 and 3) the slope of the D^*/d_m versus Pe plotted in Figure 11.

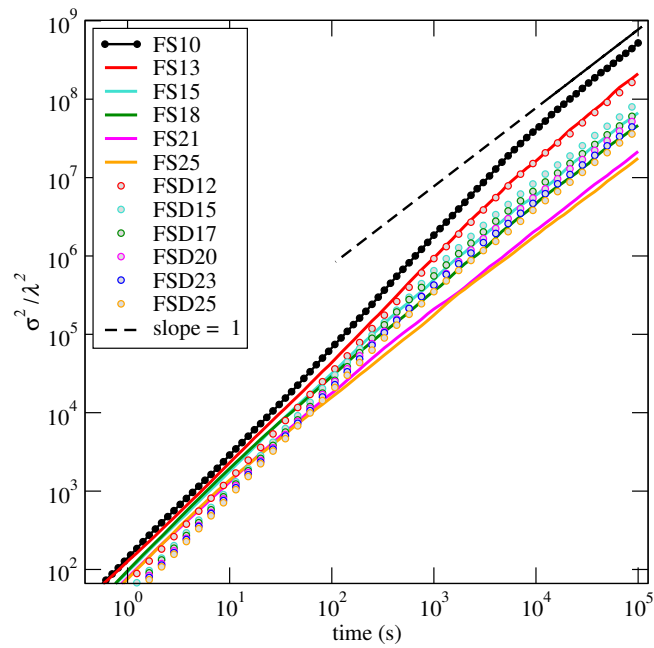


Figure 10. Normalized z -direction displacement variance versus time for $Pe = 100$.

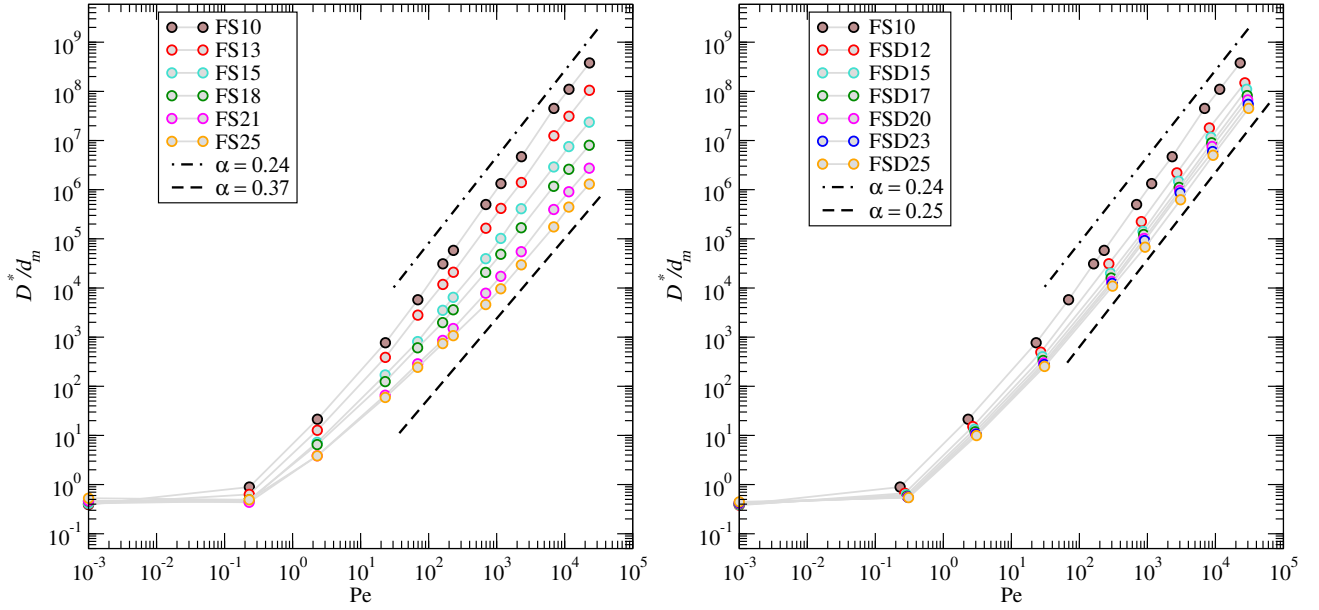


Figure 11. Asymptotic dispersion coefficient versus Pe for the FS and FSD samples

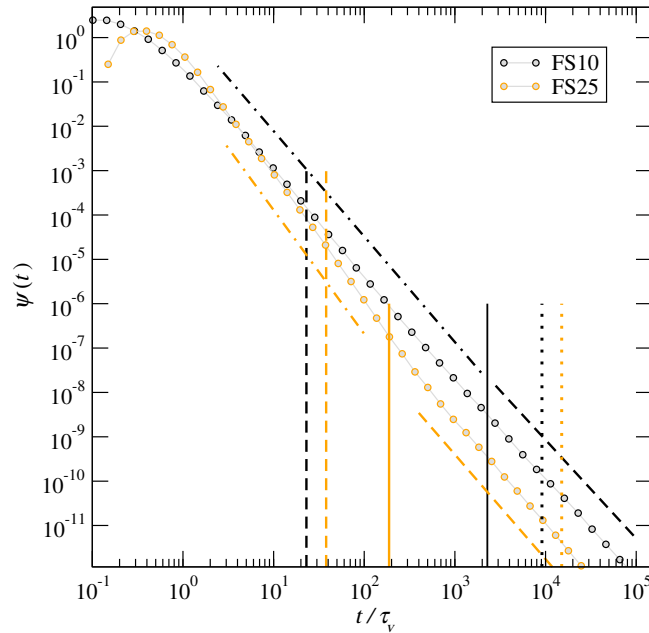


Figure 12. Distribution of advective transition times rescaled by τ_v for $FS10$ and $FS25$. The dimensionless cut-off time is $Pe = \tau_D/\tau_v$. The vertical lines denote $Pe = 10$ (dashed lines), $Pe = Pe_c$ (solid lines) and $Pe = 4000$ (dot line). The sloped lines denote the power-law behaviors $t^{-2-\alpha'}$ for $Pe < Pe_c$ with $\alpha' = 0.38$ and 0.79 for $FS10$ and $FS25$, respectively and $t^{-2-\alpha}$ for $Pe \geq Pe_c$ with $\alpha = 0.23$ and 0.37 for $FS10$ and $FS25$, respectively.